How to cite: *Angew. Chem. Int. Ed.* **2023,** *62,* e202302534
doi.org/10.1002/anie.202302534

Graphene Nanoribbons | Hot Paper

Magnetism in Nonplanar Zigzag Edge Termini of Graphene Nanoribbons

Xiushang Xu[+], Kewei Sun[+], Atsushi Ishikawa, Akimitsu Narita,* and Shigeki Kawai**

Abstract: Graphene nanoribbons (GNRs) and nanographenes synthesized by on-surface reactions using tailor-made molecular precursors offer an ideal playground for a study of magnetism towards nano-spintronics. Although the zigzag edge of GNRs has been known to host magnetism, the underlying metal substrates usually veil the edge-induced Kondo effect. Here, we report the on-surface synthesis of unprecedented, π-extended 7-armchair GNRs using 7-bromo-12-(10-bromoanthracen-9-yl)tetraphene as the precursor. Characterization by scanning tunneling microscopy/spectroscopy revealed unique rearrangement reactions leading to pentagon- or pentagon/heptagon-incorporated, nonplanar zigzag termini, which demonstrated Kondo resonances even on bare Au(111). Density functional theory calculations indicate that the nonplanar structure significantly reduces the interaction between the zigzag terminus and the Au(111) surface, leading to a recovery of the spin localization of the zigzag edge. Such a distortion of planar GNR structures offers a degree of freedom to control the magnetism on metal substrates.

Introduction

Quasi-one-dimensional graphene nanoribbons (GNRs) and zero-dimensional nanographenes (NGs) have attracted tremendous attention from researchers in the past decade since they are expected to offer key elements in forthcoming nano-electronics due to their tunable electronic properties that are dependent on the sizes and edge structures as well as substituted heteroatoms.[1] To date, various GNRs[2] and NGs[3] with atomically defined structures have been synthesized on surfaces and directly visualized by high-resolution scanning probe microscopy.[4] In the synthesis processes, designer precursor molecules are deposited on a surface and subsequently planarized by annealing, namely by surface-assisted cyclodehydrogenation. Direct planarization of precursor molecules leads to the formation of NGs, while GNRs can be obtained by functionalizing them with halogens to enable polymerization before planarization.

Besides the electronic band gap engineering, the magnetic properties can be induced in GNRs and NGs[1e,5] as the spin polarization arises from the unpaired electrons[6] and the zigzag terminal structures.[7] From the early studies of the $N=7$ armchair GNR (7-AGNR), it has been known that the zigzag terminus hosts a net spin.[2b,8] However, such magnetic property is usually suppressed by the strong interaction between the zigzag terminus and the metal substrate.[9] When 7-AGNR is successfully transferred onto an insulating surface, such as a NaCl bilayer film on Au(111) by the tip-induced manipulation, the spin splitting at the zigzag terminus can be detected by scanning tunneling spectroscopy (STS) at low temperature.[2c,10] This spin splitting of the zigzag terminus was interpreted as Coulomb gap arising from the electron-electron interaction.[6a,d] In contrast, Kondo effect relates to the magnetic moment screened by conduction electrons of a metal substrate. So far, Kondo resonances have been investigated in a few NGs and their dimers, demonstrating significant structure-dependence of their magnetic properties.[1d,6c,e,7a,11] Substituted boron atoms in 7-GNRs induce the apparent zigzag termini, leading to Kondo resonances if the interaction to the substrate is reduced by the tip lifting[6c] and the AuSix decoupling layer.[12] However, the detection of Kondo peak from GNRs on bare metal substrates still remains challenging,

[*] X. Xu,[+] A. Narita
Organic and Carbon Nanomaterials Unit,
Okinawa Institute of Science and Technology Graduate University
1919-1 Tancha, Onna-son, Kunigami-gun,
Okinawa, 904-0495 (Japan)
E-mail: akimitsu.narita@oist.jp

K. Sun,[+] S. Kawai
Research Center for Advanced Measurement and Characterization,
National Institute for Materials Science (NIMS)
1-2-1 Sengen, Tsukuba, Ibaraki, 305-0044 (Japan)
E-mail: KAWAI.Shigeki@nims.go.jp

A. Ishikawa
Center for Green Research on Energy and Environmental Materials (GREEN), National Institute for Materials Science (NIMS)
Namiki 1-1, Tsukuba, Ibaraki, 305-0044 (Japan)
and
Present address: Department of Transdisciplinary Science and Engineering, School of Environment and Society, Tokyo Institute of Technology,
2-12-1 Ookayama, Meguro-ku, Tokyo, 152-8552 (Japan)
E-mail: ishikawa.a.ai@m.titech.ac.jp

S. Kawai
Graduate School of Pure and Applied Sciences,
University of Tsukuba
Tsukuba, 305-8571 (Japan)

[+] These authors contributed equally to this work.

and thus far only achieved with chiral (3,1)-GNR upon fusion to form junctions with rearranged structures, hosting localized spins,[7d] or after a rather random introduction of carbonyl groups on zigzag edges, e.g. through exposure to oxygen gas.[13]

Herein, we report the on-surface synthesis of π-extended 7-AGNRs with nonplanar zigzag termini, which exhibits the Kondo effect on Au(111), using 7-bromo-12-(10-bromoanthracen-9-yl)tetraphene (DBATP) as the precursor. After the Ullmann-type coupling reaction on Au(111), a three-dimensional (3D) helical segment was observed as an intermediate by controlling the annealing temperature. Subsequently, the cyclodehydrogenation reaction yielded benzo- and indeno-fused 7-AGNR (BI-7-AGNR), involving skeletal rearrangement. In the planarization process, the cleavage and formation of the C–C bond at the armchair edge were systematically induced. Remarkably, we found a strong zero-bias peak at the terminus with a nonplanar structure in the vicinity of the zigzag edge. Moreover, density functional theory (DFT) calculations revealed that structural nonplanarity reduces the interaction between the zigzag edge and the meal substrate, leading to a recovery of the spin polarization.

Results and Discussion

Our original motivation was the fabrication of helical 3D-GNR[14] on a metal surface, and DBATP **1** was designed as the precursor based on 10,10′-dibromo-9,9′-bianthryl (DBBA), which has been commonly used for the synthesis of 7-AGNRs.[2b] DBATP **1** features an additional benzene ring fused to DBBA, and was expected to provide 3D-GNRs with helical segments by Ullmann-type coupling and cyclodehydrogenation on surface (Scheme 1). For the synthesis of DBATP **1**, 2-(naphthalen-2-ylmethyl)benzaldehyde

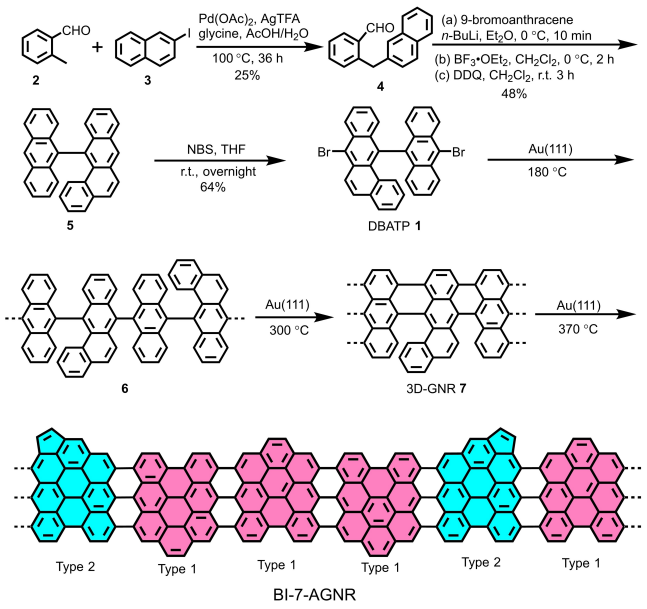

Scheme 1. The synthetic route to DBATP **1** in solution and on-surface synthesis of BI-7-AGNR.

(**4**) was initially prepared by palladium-catalyzed C(sp^3)-H arylation of 2-methylbenzaldehyde (**2**) with 2-iodonaphthalene (**3**) in 25 % yield (Scheme 1).[15] Subsequently, **4** was reacted with anthracen-9-yllithium that was generated by lithiation of 9-bromoanthracene, to give a secondary alcohol intermediate, followed by cyclization with $BF_3{\cdot}OEt_2$ and then oxidation with 2,3-dichloro-5,6-dicyano-1,4-benzoquinone (DDQ) to provide 12-(anthrancen-9-yl)tetraphene (**5**) in 48 % yield. Finally, DBATP **1** was obtained by bromination of **5** with *N*-bromosuccinimide (NBS) in 64 % yield and characterized by ^1H and ^{13}C nuclear magnetic resonance (NMR) spectroscopy and high-resolution mass spectrometry (see Supporting Information, Figures S1–S6).

Toward the on-surface synthesis of 3D-GNRs, DBATP **1** was deposited on Au(111) kept at room temperature, and subsequently annealed at 180 °C to induce the debromination and the C–C coupling. Corrugated oligomers were observed on the surface as indicated by arrows in Figure 1a, which appeared almost identical to the intermediate product in the synthesis of 7-AGNR.[2b] The successful covalent bond formation was confirmed by the tip-induced manipulation (Figure S7), which displayed the bending of the linear oligomer **6**. Higher temperature annealing at 300 °C led to the formation of planar ribbons, which has a small number of corrugated moieties with a bright feature as indicated by an arrow in Figure 1b. Since the contrast of the bright dot differs from that of 7-AGNR synthesized by imperfect cyclodehydrogenation,[16] it can be readily assigned to an extra benzene ring originally existing in the structure of DBATP (Figure S8). Thus, the 3D-helical segment **7** was successfully incorporated in the edges of GNRs, which has never been reported before to the best of our knowledge. However, most of the parts in the ribbon became flat, suggesting the occurrence of strain-induced skeletal rearrangement.[17] After heating the sample to 370 °C, completely planar GNRs without bright dots appeared on surface as indicated by arrows in Figure 1c. Figure 1d shows the close view of the GNR, in which both sides in the longitudinal axis have irregular nodes as marked by arrows. To investigate the structures, the tip apex was terminated with a CO molecule[18] and was scanned at a constant height over the GNR while recoding the differential conductance dI/dV (Figure 1e). The contrast at the terminus is much brighter than those of other parts of the GNR, which has already indicated the presence of the spin-polarized state at the terminus. We first focus on the edges of the longitudinal axis as indicated by a rectangle in Figure 1e. The inner structure of the GNR segment was clearly observed in the bond-resolved dI/dV map (Figure 1f), in which the extra benzene rings from the DBATP precursor were not visible. We instead found a systematic rearrangement of carbon atoms, consequently forming two types of structures; (i) one hexagonal ring (Type 1) and (ii) a set of hexagonal and pentagonal rings (Type 2) fused to the armchair edges (Figure S26), leading to benzo- and indeno-fused 7-AGNR (BI-7-AGNR). The chemical structures of Type 1 and Type 2 have been defined in Scheme 1. For a better observation, the close-up bond-resolved image of Type 1 and Type 2 was recorded as shown in Figure S9. Additional

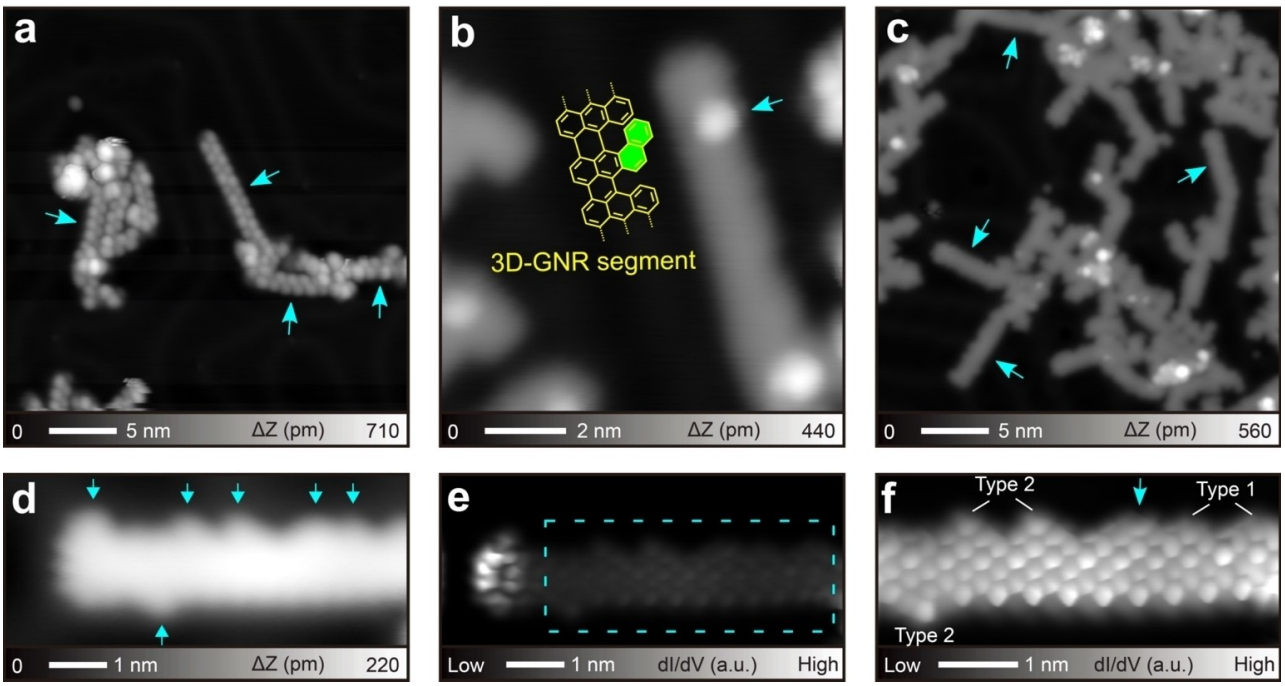

Figure 1. On-surface synthesis of BI-7-AGNR on Au(111). a) STM topography of DBATP on Au(111) after annealing to 180 °C for 10 min. b) STM topography of the surface after heating to 300 °C for 10 min. The inset shows the structural model of a 3D-GNR segment. c) STM overview of the surface after heating to 370 °C for 10 min. d) Close-up view of BI-7-AGNR on Au(111) and e) the corresponding constant height d*I*/d*V* map. f) Constant height d*I*/d*V* map of the area indicated by a rectangle in (e). Measurement parameters: Sample bias voltage $V = 200$ mV and tunneling current $I = 5$ pA in (a, b, c). $V = 200$ mV and $I = 3$ pA in (d). For constant height d*I*/d*V* map: $V = 1$ mV, $V_{ac} = 10$ mV in (e, f).

images of other GNR segments are displayed in Figure S10. Type 1 has two carbon atoms less compared with the precursor, which might be removed as ethylene or ethane. We also found that this ethenylene can occasionally fuse to the adjacent armchair edge of GNR (Figure S10). We assume that the reaction mechanism leading to Types 1 and 2 might be similar to the reaction pathway that was previously proposed for a related system,[17] but consider that in-depth theoretical studies would be necessary for further discussion.[19,20] Another edge site (indicated by light blue arrow in Figure 1f) appeared different from Type 1 and Type 2, and we propose the corresponding chemical structure as shown in Figure S11.

Given the fact that the BI-7-AGNR lack periodic edges, the electronic structures measured by STS were rather complicated. A series of the d*I*/d*V* curves were taken along the longitudinal axes of GNR and showed a strong modification of electronic structures by the nodes. Such electronic structures were also seen in d*I*/d*V* maps taken at different bias voltages (Figure S12).

In the vicinity of the zigzag termini of the GNRs, we observed three different structures. Figure 2a shows a close-up view of the first type of the terminus, in which a small node is indicated by an arrow. The constant height d*I*/d*V* map (Figure 2b) and the corresponding Laplace filtered image (Figure 2c) show the distinct inner structure, in which the formation of the additional hexagonal ring can be observed (Figure 2d). Hereafter, we name this terminus as Terminal 1. Figure 2e shows the second type of the terminus with a larger node in the STM topography as indicated by an arrow. The corresponding chemical structure was identified from the constant height d*I*/d*V* maps (Figure 2f, Figure S13) and the Laplace filtered image (Figure 2g), named as Terminal 2 (Figure 2h). The large node in the STM topography is related to the apparent feature of the pentagonal ring and the hexagonal ring. Unlike the bare 7-AGNR directly adsorbed on Au(111), strong contrasts were detected at the zigzag edge. The structure of Terminal 2 appeared similar to that of Type 2, but the positions of the pentagonal and hexagonal rings were switched each other (see also Figure S26). Consequently, the additional hexagonal ring at the zigzag edge is slightly pulled towards the GNR main body by the small pentagonal ring. Figure 2i shows the last terminus, having two small nodes as marked by arrows, named as Terminal 3. We found the strong signal in the constant height d*I*/d*V* map around the nodes, indicating the corrugated structure (Figure 2j, Figure S14). According to the corresponding Laplace filtered image (Figure 2k), in which one heptagonal ring and two adjacent pentagonal rings are visible, we assign Terminal 3 to the chemical structure as shown in Figure 2l. We also observed a similar structure within a GNR segment (called Type 3 in Figure S10d), supporting this structural assignment. Interestingly, for Terminals 2 and 3, the constant height d*I*/d*V* maps taken at close to the Fermi level (Figure 2f and g) show significant modulations of the differential conductance. This phenomenon suggests the presence of spin-polarized states,

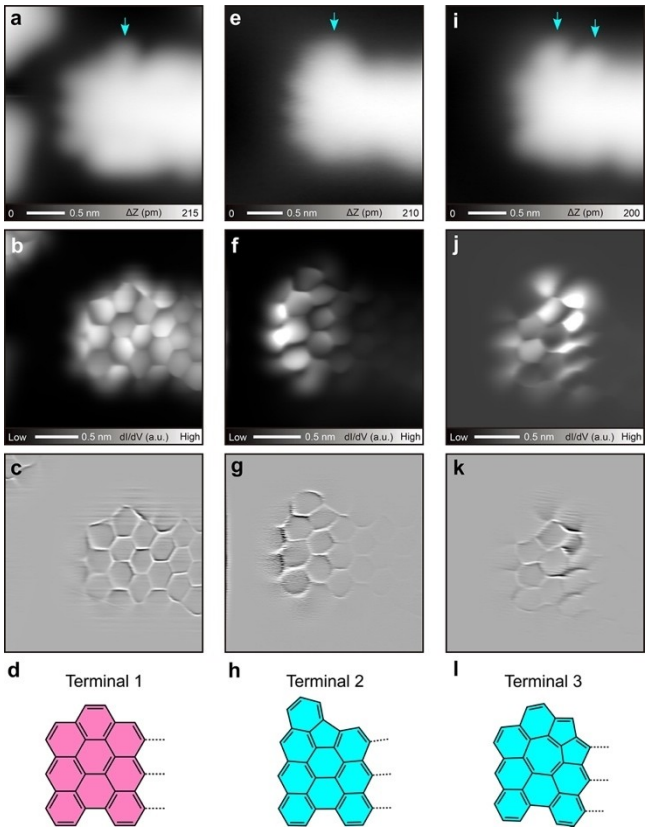

Figure 2. Three types of termini structures of BI-7-AGNR on Au(111). a) STM topography of Terminal 1 with a small node (indicated by an arrow) at the top edge of BI-7-AGNR. b) Constant height d*I*/d*V* map of one Terminal 1. c) Corresponding Laplace filtered image. d) Corresponding chemical structure. e) STM topography Terminal 2 with a large node (indicated by an arrow) at the top edge of BI-7-AGNR. f) Constant height d*I*/d*V* map of Terminal 2. g) Corresponding Laplace filtered image. h) Corresponding chemical structure. i) STM topography of Terminal 3 with two small nodes at the top edge of BI-7-AGNR. j) Constant height d*I*/d*V* map of Terminal 3. k) Corresponding chemical structure. l) Corresponding chemical structure. STM measurement parameters: $V=200$ mV and $I=5$ pA in (a, i). $V=200$ mV and $I=3$ pA in (e). For constant height d*I*/d*V* maps: $V=1$ mV, $V_{ac}=10$ mV in (b, f). $V=0$, $V_{ac}=1$ mV in (j).

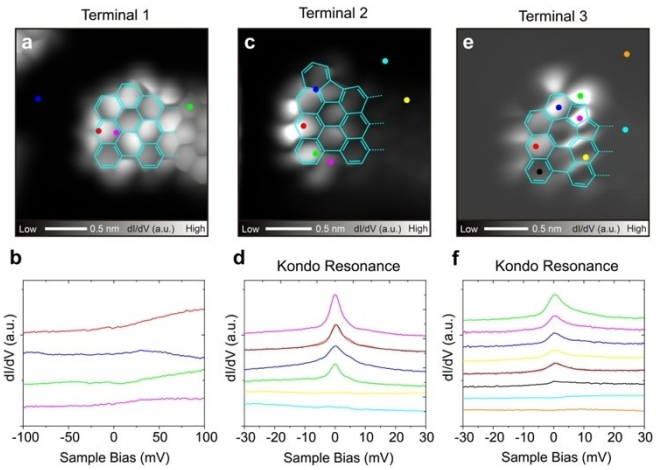

Figure 3. STS characterization of three types of termini structures. a) Bond-resolved image of Terminal 1 with the chemical structure superimposed. b) d*I*/d*V* curves recorded at different sites as indicated by the colored dots in (a). c) Bond-resolved image of Terminal 2 with the chemical structure superimposed. d) d*I*/d*V* curves measured at different sites as indicated by the colored dots in (c). e) Bond-resolved image of Terminal 3 with the chemical structure superimposed. f) d*I*/d*V* curves measured at different sites as indicated by the colored dots in (f). The dashed lines overlapping the red lines in (d) and (f) were obtained from Frota fitting. The bond-resolved images in (a, c, e) are identical with Figure 2b, f and j, respectively. Measurement parameters: For constant height d*I*/d*V* maps: $V=1$ mV, $V_{ac}=10$ mV in (a, c). $V=0$, $V_{ac}=1$ mV in (e). $V=100$ mV, $I=100$ pA, $V_{ac}=1$ mV for STS in (b). $V=30$ mV, $I=200$ pA, $V_{ac}=0.3$ mV for STS in (d). $V=30$ mV, $I=100$ pA, $V_{ac}=0.3$ mV for STS in (f).

which is usually quenched by the interaction between the zigzag terminus of GNR and the underlying Au(111).

To investigate the origin of the bright contrast at the modified termini of the GNRs on Au(111), the electronic structures with large energy ranges (Figure S15) and near the Fermi level (Figure 3) were measured with STS. Figure 3a shows a bond-resolved image of Terminal 1, superimposed with the structural model and dots, which indicates the tip positions for the STS measurements. We observed the absence of the zero-bias peak in the d*I*/d*V* curves (Figure 3b), meaning that no net spin exists in Terminal 1. This result is consistent with that of non-decorated 7-AGNR edge. In contrast, distinct zero-bias peaks appeared at the zigzag edge of Terminal 2 as indicated by the red dot and curve in Figures 3c and d, respectively. Furthermore, similar peaks were also measured near the zigzag edge as indicated by green, blue, and pink curves. We assigned the zero-bias state to Kondo resonance, arising from the magnetic moment screened by conduction electrons of the Au(111) surface, since such a peak was absent at the site distant from the zigzag edge (light blue and yellow). We found that Terminal 3 also shows a zero-bias peak in the d*I*/d*V* curves (Figures 3e and f). In contrast, the d*I*/d*V* curve above the pentagonal ring fused at armchair edge far away from the zigzag terminus has no zero-bias peak (Figure S16), indicating pentagonal ring itself could not hold net spin. Given that the zigzag terminus of a GNR can increase its interaction with the underlying substrate due to formation of a single C–Au bond after removing a hydrogen (H) atom,[21] this behavior would quench the spin polarization. Thus, we utilized the tip manipulation to remove one H atom at the zigzag termini of Terminal 2 and 3 and found the disappearance of the zero-bias peak (Figures S17 and S18). These results further suggest that the GNR spin density arises from the zigzag edges. Half width at half maximum (HWHM) of the curve at the zigzag edge of Terminal 3 obtained by Frota fitting (indicated by dashed lines in Figure 3d and f) is 12.7 ± 0.8 mV, while that of Terminal 2 is 2.7 ± 0.3 mV. The larger linewidth of Terminus 3 might be because of its relatively strong interaction with the underlying substrate. Nevertheless, the net spin is no longer suppressed by the Au(111) substrate regardless of whether the end of GNR is Terminal 2 or Terminal 3. These types of termini were observed also in some other GNRs, and the corresponding STS measurements displayed the consistent results that Terminal 2 and 3 have zero-bias peak (Figures S19–S21). Our study demonstrates the importance of edge

modification to GNR, which is expected to effectively decouple GNR from metal substrate, e.g. indeno-fused zigzag-GNR on Au(111).[2c]

To study the structure and the electronic state of the GNR adsorbed on Au(111) in depth, DFT calculations were carried out as they provide key factors for understanding the experimental results, especially the zero-bias peak in Figure 3. Figures 4a and b show the optimized geometry of the BI-7-AGNR with 4 units containing Terminal 2 (see also Figure S22) and the corresponding spin density, respectively. We found the spin density localized around the left terminal of the GNR, which is in agreement with the experimental result in Figure 3c. The side view of the DFT optimized structure (Figure 4a) shows that the adsorption height of the zigzag edge is slightly larger than that of the rest; the unit with the edge has a mean adsorption height of 2.65 Å while that of the whole GNR is 2.35 Å. Such corrugated structure reduces the interaction between the zigzag edge and the underlying gold substrate. The more specific details about gaps between GNR and substrate can be seen in Figure S23, in which the z-position (perpendicular to the Au(111) surface) of the C atoms is plotted in the bar chart. To investigate the origin of spin density, we performed DFT calculations on periodic GNR with a pentagon ring fused at the bulk edge (Figure S24), showing almost no spin density. The spin densities of Terminals 1 and 3 were also calculated and the results are displayed in Figure S25. DFT calculations indicated that Terminal 1 exhibits a negligible spin density, while the relatively strong spin density for Terminal 3 were observed. Terminal 3 displays more delocalized spin density than that of Terminal 2. Thus, Terminal 2 exhibits the highest zero-bias peak, Terminal 3 lower zero-bias peak, and Terminal 1 no peak, which is in good agreement with the experimental results (Figure 3). To further analyze the relationship between spin density and the GNR-Au(111) interaction, the GNR terminus was artificially lifted by 1.78–3.28 Å (Figures 4c). The distribution plot clearly shows that spin density around the GNR terminus significantly enhances with increasing the adsorption height. Thus, DFT calculations revealed that Terminal 2 and 3 are significantly nonplanar, increasing their adsorption height on Au(111), which decreases the interaction between GNR termini and Au(111) surface, and recovers the spin polarization.

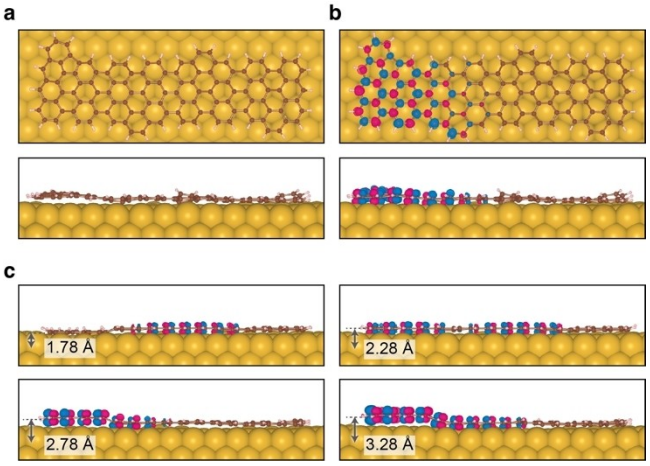

Figure 4. DFT calculations of the GNR segment on Au(111). a) Optimized geometry. b) Spin density at the optimized geometry. The upper and lower Figures show the top and side views, respectively. c) Spin density at the optimized GNR segments at different distances from the Au(111) surface of 1.78–3.28 Å. The spin density isosurface of 3×10^{-3} e is used for all plots.

Conclusion

In summary, we demonstrate a synthesis of π-extended 7-AGNR with unique edge and termini structures using 7-bromo-12-(10-bromoanthracen-9-yl)tetraphene as the precursor on Au(111). During the process of annealing, we observed the appearance of 3D-GNR with [6]helicene substructures. Further annealing resulted in the formation of planarized BI-7-AGNR with three type of termini structures, involving strain-induced skeletal rearrangement at the [6]helicene moieties. A Kondo resonance appeared even on a bare Au(111) surface for nonplanar zigzag termini, which may allow further investigations of the magnetic properties of the GNRs. DFT calculations revealed that terminal structural deformation induced a decoupling from the substrate, restoring the spin polarization. Although further optimization of the precursor structure is necessary for obtaining GNRs with uniformly fused helicenes, we believe that these results pave the way toward the synthesis of other 3D-GNRs with helicene-incorporated edge structures. Moreover, the introduction of the local structural deformation may be the key to realizing magnetic properties of other carbon-based materials on metal substrates.

Acknowledgements

This work was financially supported in part by Japan Society for the Promotion of Science (JSPS) KAKENHI Grant Numbers 19K24686, 21K18885, 21F21058, and 22H00285, and the Okinawa Institute of Science and Technology Graduate University. We appreciate the help and support provided by the Instrumental Analysis Section of Research Support Division at OIST.

Conflict of Interest

The authors declare no conflict of interest.

Data Availability Statement

The data that support the findings of this study are available from the corresponding author upon reasonable request.

Keywords: Graphene Nanoribbons · On-Surface Synthesis · Scanning Tunneling Microscopy · Spin Polarization · Zigzag Termini

[1] a) Y. Yano, N. Mitoma, H. Ito, K. Itami, *J. Org. Chem.* **2020**, *85*, 4–33; b) A. Borissov, Y. K. Maurya, L. Moshniaha, W.-S. Wong, M. Żyła-Karwowska, M. Stępień, *Chem. Rev.* **2022**, *122*, 565–788; c) Z. Liu, S. Fu, X. Liu, A. Narita, P. Samorì, M. Bonn, H. I. Wang, *Adv. Sci.* **2022**, *9*, 2106055; d) D. Jacob, R. Ortiz, J. Fernández-Rossier, *Phys. Rev. B* **2021**, *104*, 075404; e) S. Song, J. Su, M. Telychko, J. Li, G. Li, Y. Li, C. Su, J. Wu, J. Lu, *Chem. Soc. Rev.* **2021**, *50*, 3238–3262; f) J. Li, Y. Hu, L. Yu, L. Li, D. Ji, L. Li, W. Hu, H. Fuchs, *Small* **2021**, *17*, 2100724; g) R. Kawaguchi, K. Hashimoto, T. Kakudate, K. Katoh, M. Yamashita, T. Komeda, *Nano Lett.* **2023**, *23*, 213–219.

[2] a) L. Talirz, P. Ruffieux, R. Fasel, *Adv. Mater.* **2016**, *28*, 6222–6231; b) J. Cai, P. Ruffieux, R. Jaafar, M. Bieri, T. Braun, S. Blankenburg, M. Muoth, A. P. Seitsonen, M. Saleh, X. Feng, K. Müllen, R. Fasel, *Nature* **2010**, *466*, 470–473; c) P. Ruffieux, S. Wang, B. Yang, C. Sánchez-Sánchez, J. Liu, T. Dienel, L. Talirz, P. Shinde, C. A. Pignedoli, D. Passerone, T. Dumslaff, X. Feng, K. Müllen, R. Fasel, *Nature* **2016**, *531*, 489–492; d) Y.-C. Chen, D. G. de Oteyza, Z. Pedramrazi, C. Chen, F. R. Fischer, M. F. Crommie, *ACS Nano* **2013**, *7*, 6123–6128; e) H. Zhang, H. Lin, K. Sun, L. Chen, Y. Zagranyarski, N. Aghdassi, S. Duhm, Q. Li, D. Zhong, Y. Li, K. Müllen, H. Fuchs, L. Chi, *J. Am. Chem. Soc.* **2015**, *137*, 4022–4025; f) L. Talirz, H. Söde, T. Dumslaff, S. Wang, J. R. Sanchez-Valencia, J. Liu, P. Shinde, C. A. Pignedoli, L. Liang, V. Meunier, N. C. Plumb, M. Shi, X. Feng, A. Narita, K. Müllen, R. Fasel, P. Ruffieux, *ACS Nano* **2017**, *11*, 1380–1388; g) J. Liu, B.-W. Li, Y.-Z. Tan, A. Giannakopoulos, C. Sanchez-Sanchez, D. Beljonne, P. Ruffieux, R. Fasel, X. Feng, K. Müllen, *J. Am. Chem. Soc.* **2015**, *137*, 6097–6103; h) P. Han, K. Akagi, F. Federici Canova, H. Mutoh, S. Shiraki, K. Iwaya, P. S. Weiss, N. Asao, T. Hitosugi, *ACS Nano* **2014**, *8*, 9181–9187; i) S. Kawai, S. Saito, S. Osumi, S. Yamaguchi, A. S. Foster, P. Spijker, E. Meyer, *Nat. Commun.* **2015**, *6*, 8098; j) S. Clair, D. G. de Oteyza, *Chem. Rev.* **2019**, *119*, 4717–4776; k) X. Liu, G. Li, A. Lipatov, T. Sun, M. Mehdi Pour, N. R. Aluru, J. W. Lyding, A. Sinitskii, *Nano Res.* **2020**, *13*, 1713–1722; l) Q. Fan, L. Yan, M. W. Tripp, O. Krejčí, S. Dimosthenous, S. R. Kachel, M. Chen, A. S. Foster, U. Koert, P. Liljeroth, J. M. Gottfried, *Science* **2021**, *372*, 852–856; m) Q. Fan, D. Martin-Jimenez, D. Ebeling, C. K. Krug, L. Brechmann, C. Kohlmeyer, G. Hilt, W. Hieringer, A. Schirmeisen, J. M. Gottfried, *J. Am. Chem. Soc.* **2019**, *141*, 17713–17720.

[3] a) M. Treier, C. A. Pignedoli, T. Laino, R. Rieger, K. Müllen, D. Passerone, R. Fasel, *Nat. Chem.* **2011**, *3*, 61–67; b) C. Rogers, C. Chen, Z. Pedramrazi, A. A. Omrani, H.-Z. Tsai, H. S. Jung, S. Lin, M. F. Crommie, F. R. Fischer, *Angew. Chem. Int. Ed.* **2015**, *54*, 15143–15146; c) Q. Fan, D. Martin-Jimenez, S. Werner, D. Ebeling, T. Koehler, T. Vollgraff, J. Sundermeyer, W. Hieringer, A. Schirmeisen, J. M. Gottfried, *J. Am. Chem. Soc.* **2020**, *142*, 894–899.

[4] a) L. Grill, S. Hecht, *Nat. Chem.* **2020**, *12*, 115–130; b) L. Grill, M. Dyer, L. Lafferentz, M. Persson, M. V. Peters, S. Hecht, *Nat. Nanotechnol.* **2007**, *2*, 687–691.

[5] J. Fernández-Rossier, J. J. Palacios, *Phys. Rev. Lett.* **2007**, *99*, 177204.

[6] a) S. Mishra, D. Beyer, K. Eimre, J. Liu, R. Berger, O. Gröning, C. A. Pignedoli, K. Müllen, R. Fasel, X. Feng, P. Ruffieux, *J. Am. Chem. Soc.* **2019**, *141*, 10621–10625; b) J. Su, M. Telychko, P. Hu, G. Macam, P. Mutombo, H. Zhang, Y. Bao, F. Cheng, Z.-Q. Huang, Z. Qiu, S. J. R. Tan, H. Lin, P. Jelínek, F.-C. Chuang, J. Wu, J. Lu, *Sci. Adv.* **2019**, *5*, eaav7717; c) J. Li, S. Sanz, J. Castro-Esteban, M. Vilas-Varela, N. Friedrich, T. Frederiksen, D. Peña, J. I. Pascual, *Phys. Rev. Lett.* **2020**, *124*, 177201; d) Q. Sun, X. Yao, O. Gröning, K. Eimre, C. A. Pignedoli, K. Müllen, A. Narita, R. Fasel, P. Ruffieux, *Nano Lett.* **2020**, *20*, 6429–6436; e) Y. Zheng, C. Li, C. Xu, D. Beyer, X. Yue, Y. Zhao, G. Wang, D. Guan, Y. Li, H. Zheng, C. Liu, J. Liu, X. Wang, W. Luo, X. Feng, S. Wang, J. Jia, *Nat. Commun.* **2020**, *11*, 6076.

[7] a) S. Mishra, D. Beyer, K. Eimre, S. Kezilebieke, R. Berger, O. Gröning, C. A. Pignedoli, K. Müllen, P. Liljeroth, P. Ruffieux, X. Feng, R. Fasel, *Nat. Nanotechnol.* **2020**, *15*, 22–28; b) E. Turco, S. Mishra, J. Melidonie, K. Eimre, S. Obermann, C. A. Pignedoli, R. Fasel, X. Feng, P. Ruffieux, *J. Phys. Chem. Lett.* **2021**, *12*, 8314–8319; c) S. Mishra, X. Yao, Q. Chen, K. Eimre, O. Gröning, R. Ortiz, M. Di Giovannantonio, J. C. Sancho-García, J. Fernández-Rossier, C. A. Pignedoli, K. Müllen, P. Ruffieux, A. Narita, R. Fasel, *Nat. Chem.* **2021**, *13*, 581–586; d) J. Li, S. Sanz, M. Corso, D. J. Choi, D. Peña, T. Frederiksen, J. I. Pascual, *Nat. Commun.* **2019**, *10*, 200.

[8] M. Ijäs, M. Ervasti, A. Uppstu, P. Liljeroth, J. van der Lit, I. Swart, A. Harju, *Phys. Rev. B* **2013**, *88*, 075429.

[9] P. Ruffieux, J. Cai, N. C. Plumb, L. Patthey, D. Prezzi, A. Ferretti, E. Molinari, X. Feng, K. Müllen, C. A. Pignedoli, R. Fasel, *ACS Nano* **2012**, *6*, 6930–6935.

[10] S. Wang, L. Talirz, C. A. Pignedoli, X. Feng, K. Müllen, R. Fasel, P. Ruffieux, *Nat. Commun.* **2016**, *7*, 11507.

[11] a) S. Mishra, D. Beyer, R. Berger, J. Liu, O. Gröning, J. I. Urgel, K. Müllen, P. Ruffieux, X. Feng, R. Fasel, *J. Am. Chem. Soc.* **2020**, *142*, 1147–1152; b) J. Lawrence, P. Brandimarte, A. Berdonces-Layunta, M. S. G. Mohammed, A. Grewal, C. C. Leon, D. Sánchez-Portal, D. G. de Oteyza, *ACS Nano* **2020**, *14*, 4499–4508.

[12] K. Sun, O. J. Silveira, S. Saito, K. Sagisaka, S. Yamaguchi, A. S. Foster, S. Kawai, *ACS Nano* **2022**, *16*, 11244–11250.

[13] T. Wang, S. Sanz, J. Castro-Esteban, J. Lawrence, A. Berdonces-Layunta, M. S. G. Mohammed, M. Vilas-Varela, M. Corso, D. Peña, T. Frederiksen, D. G. de Oteyza, *Nano Lett.* **2022**, *22*, 164–171.

[14] S. Kawai, O. Krejčí, T. Nishiuchi, K. Sahara, T. Kodama, R. Pawlak, E. Meyer, T. Kubo, A. S. Foster, *Sci. Adv.* **2020**, *6*, eaay8913.

[15] F.-L. Zhang, K. Hong, T.-J. Li, H. Park, J.-Q. Yu, *Science* **2016**, *351*, 252–256.

[16] S. Blankenburg, J. Cai, P. Ruffieux, R. Jaafar, D. Passerone, X. Feng, K. Müllen, R. Fasel, C. A. Pignedoli, *ACS Nano* **2012**, *6*, 2020–2025.

[17] O. Stetsovych, M. Švec, J. Vacek, J. V. Chocholoušová, A. Jančařík, J. Rybáček, K. Kosmider, I. G. Stará, P. Jelínek, I. Starý, *Nat. Chem.* **2017**, *9*, 213–218.

[18] a) R. Temirov, S. Soubatch, O. Neucheva, A. C. Lassise, F. S. Tautz, *New J. Phys.* **2008**, *10*, 053012; b) L. Gross, F. Mohn, N. Moll, P. Liljeroth, G. Meyer, *Science* **2009**, *325*, 1110–1114.

[19] J. Björk, C. Sánchez-Sánchez, Q. Chen, C. A. Pignedoli, J. Rosen, P. Ruffieux, X. Feng, A. Narita, K. Müllen, R. Fasel, *Angew. Chem. Int. Ed.* **2022**, *61*, e202212354.

[20] A. Kinikar, M. Di Giovannantonio, J. I. Urgel, K. Eimre, Z. Qiu, Y. Gu, E. Jin, A. Narita, X.-Y. Wang, K. Müllen, P. Ruffieux, C. A. Pignedoli, R. Fasel, *Nat. Synth.* **2022**, *1*, 289–296.

[21] J. van der Lit, M. P. Boneschanscher, D. Vanmaekelbergh, M. Ijäs, A. Uppstu, M. Ervasti, A. Harju, P. Liljeroth, I. Swart, *Nat. Commun.* **2013**, *4*, 2023.

Manuscript received: February 19, 2023
Accepted manuscript online: March 16, 2023
Version of record online: April 13, 2023